# On the limits of quasi-static theory in plasmonic nanostructures

Giulia Crotti[1,2], Andrea Schirato[1,2], Remo Proietti Zaccaria[2,3], and Giuseppe Della Valle[1,4,5]*
[1] *Dipartimento di Fisica - Politecnico di Milano, Piazza Leonardo da Vinci, 32, I-20133 Milano, Italy,*
[2] *Istituto Italiano di Tecnologia, via Morego 30, I-16163, Genova, Italy,*
[3] *Cixi Institute of Biomedical Engineering, Ningbo Institute of Industrial Technology, Chinese Academy of Sciences, 1219 Zhongguan West Road, Ningbo 315201, China,*
[4] *Istituto di Fotonica e Nanotecnologie - Consiglio Nazionale delle Ricerche, Piazza Leonardo da Vinci, 32, I-20133 Milano, Italy,*
[5] *Istituto Nazionale di Fisica Nucleare - Sezione di Milano, Via Celoria 16, I-20133 Milano, Italy*

The approximated analytical approach of Quasi-Static Theory (QST) is widely used in modelling the optical response of plasmonic nanoparticles. It is well known that its accuracy is remarkable provided that the particle is much smaller than the wavelength of the interacting radiation and that the field induced inside the structure is approximately uniform. Here, we investigate the limits of QST range of validity for gold nanostructures freestanding in air. First, we compare QST predictions of scattering spectra of nanospheres and cylindrical nanowires of various sizes with the exact results provided by Mie scattering theory. We observe a non-monotonic behaviour of the error of QST as a function of the characteristic length of the nanostructures, revealing a non-trivial scaling of its accuracy with the scatterer size. Second, we study nanowires with elliptical section upon different excitation conditions by performing finite element numerical analysis. Comparing simulation results with QST estimates of the extinction cross-section, we find that QST accuracy is strongly dependent on the excitation conditions, yielding good results even if the field is highly inhomogeneous inside the structure.

## INTRODUCTION

Plasmonic nanoparticles (NPs) are currently employed in a vast range of applications, including chemical and biological sensing [1–4], photocatalysis [5–9], and surface-enhanced Raman spectroscopy [10, 11]. Plasmonic nanostructures also represent the building blocks for the development of unprecedented ultracompact photonic devices, from nanolasers [12], to gradient birefringent mirrors [13] and ultrafast optical modulators [14, 15], just to mention a few (see also Refs. 16–20 for an overview).

Accurate modelling of the optical response of these structures is essential to the design and fabrication of effective devices. In this context, classical electromagnetism is commonly adopted as a suitable theoretical framework. The numerical solution of Maxwell's equations provides detailed predictions on the optical properties of plasmonic systems. However, electromagnetic simulations are often computationally demanding. Exact analytical solutions, on the other hand, exist only for selected geometries of the scatterer; for example, Mie theory [21] is widely used to model the optical response of spherical nanoparticles or nanowires with circular cross-section.

In contrast, the approximated analytical approach of Quasi-Static Theory (QST) does not require computational resources and can grant remarkably accurate estimates provided that the two following conditions are satisfied [22]: the particle must be much smaller than the wavelength of the interacting light; the induced electromagnetic field must be approximately uniform inside the nanostructure. These requirements are believed to be necessary and sufficient conditions for the QST approach to be valid. Quantitatively, a smallness parameter $x$ is commonly defined to be proportional to the ratio between a characteristic size of the scatterer and the incident wavelength. The characteristic size is usually the maximum distance between two points inside the nanostructure.

The two requirements translate into inequalities involving both the smallness parameter and the ratio $m$ between the refractive indexes of the metal and the environment:

$$x \ll 1, \tag{1}$$

$$|m|x \ll 1. \tag{2}$$

These inequalities are often used as rules of thumb in framing the limits of the QST approach, and comparisons with full-wave numerical results have been reported by many authors (see, e.g. [23]). Also, QST predictions (especially in terms of the quality factor, being a universal function of materials permittivity [24]) have been widely used as benchmarks for the performance of plasmonic nanoresonators of different shapes [25–27].

However, more specific, quantitative assessments of the general limits stated by Eqs. (1)-(2) have not been thoroughly performed in literature, with the exception of a recent study specifically focused on gold and silver nanospheres [28].

In this paper, we investigate the limits of the range of QST validity for free-standing Au nanospheres and nanowires. Our general results can be extended to other kinds of metallic media such as Ag or Al.

* giuseppe.dellavalle@polimi.it

We first compare quasi-static predictions for the scattering spectra of nanospheres and cylindrical nanowires with the exact results provided by Mie theory. This analysis shows that, in a specific spectral region, the relative error of QST scales non-monotonically with the smallness parameter.

Second, we perform finite element numerical simulations to study nanowires of elliptical sections upon different electromagnetic excitation conditions, by varying the polarisation of the incident plane wave. Thus, we compare the resulting extinction spectra with the QST estimates. Our results show that QST accuracy is strongly dependent on the excitation conditions; furthermore, good agreement between simulated and quasi-static spectra is found even when the field induced inside the structures is highly inhomogeneous. We argue that this implies that conditions (1), (2) are only sufficient for the determination of the accuracy of QST. In fact, a more proper definition of the smallness parameter should take into account the excitation conditions, which have a heavy influence on the reliability of QST.

## I. RESULTS AND DISCUSSION

Mie theory provides the exact solution to the problem of plane wave scattering by a sphere of arbitrary radius and refractive index [21]. Specifically, scattering and extinction cross-sections can be written as series of the so-called Mie scattering coefficients $a_n$, $b_n$ [22]:

$$\sigma_{\text{sca}} = \frac{2\pi}{k^2}\sum_{n=1}^{\infty}(2n+1)\left(|a_n|^2+|b_n|^2\right), \tag{3}$$

$$\sigma_{\text{ext}} = \frac{2\pi}{k^2}\sum_{n=1}^{\infty}(2n+1)\,\text{Re}\left(a_n+b_n\right), \tag{4}$$

with $k = n_e k_0$ the incident light wave vector propagating in a homogeneous medium of refractive index $n_e$, $k_0 = \frac{2\pi}{\lambda}$ being the light wave vector in vacuum. In turn, the scattering coefficients are defined as functions of the smallness parameter $x = kr$, with $r$ the radius of the sphere, and of the ratio $m = n_m/n_e$ between the refractive indexes of the metal and environment, respectively. Scattering and extinction efficiencies $Q_{\text{sca}}$, $Q_{\text{ext}}$ are obtained by normalising the corresponding cross-sections to the geometrical cross-section of the particle, $A = \pi r^2$. Energy conservation allows to derive the absorption efficiency as $Q_{\text{abs}} = Q_{\text{ext}} - Q_{\text{sca}}$.

Mie theory has been extended to other problems with suitable symmetry, including two-dimensional configurations, and, notably, to infinite wires of circular cross-section. For plane wave excitation with electric field orthogonal to the wire axis (the so called in-plane p-polarisation), the cross-sections read as follows:

$$\sigma_{\text{sca}} = \frac{4}{k}\left[|c_0|^2 + 2\sum_{n=1}^{\infty}|c_n|^2\right], \tag{5}$$

$$\sigma_{\text{ext}} = \frac{4}{k}\text{Re}\left(c_0 + 2\sum_{n=1}^{\infty}c_n\right). \tag{6}$$

Again, the coefficients $c_n$ are functions of the smallness parameter $x$, defined in terms of the cylinder radius, and of the $m$ ratio.

On the other hand, the approximate analytic approach of QST consists in reducing the scattering problem of a plane monochromatic wave impinging on a nanoobject with small cross-section to an electrostatic problem. The procedure is well developed for highly symmetric configurations, including nanospheres, nanoellipsoids, cylindrical nanowires and elliptical nanowires (see methods section for the computation of the QST cross-sections of cylindrical and elliptical nanowires).

This approach implies two fundamental assumptions. The first is related to the scatterer characteristic size, $r$: if it is much smaller than the incident wavelength, the NP experiences an approximately spatially uniform field. This translates into the inequality (1) [22].

The second assumption is on the timescale $\tau$ of the variation of the incident wave; indeed, the field can be considered as *quasi-static* if the time required for wave propagation inside the particle is much smaller than $\tau$. This is assured if $n'_m x/n_e \ll 1$, where $n'_m$ is the real part of the refractive index of the nanoparticle [22].

Usually, a third condition is deemed necessary to the reliability of the QST approach: the field inside the particle is required to be approximately uniform, as in the electrostatic case. This is enforced by the inequality $n''_m x/n_e \ll 1$, where $n''_m$ is the imaginary part of the refractive index of the nanoparticle. Therefore, the constraint (2) summarises the conditions on the real and imaginary part of the refractive index of the NP.

For a sphere of radius $r$, the QST cross-sections read [22]:

$$\sigma_{\text{sca}}^{\text{QST}} = \frac{8}{3}\pi r^2 x^4\left|\frac{m^2-1}{m^2+2}\right|^2, \tag{7}$$

$$\sigma_{\text{ext}}^{\text{QST}} = 4\pi r^2 x\ \text{Im}\left(\frac{m^2-1}{m^2+2}\right) + \sigma_{\text{sca}}^{\text{QST}}. \tag{8}$$

For an infinite circular cylinder of radius $r$, illuminated at normal incidence with respect to the cylinder's axis and for in-plane polarisation defined as before, the cross-sections are

$$\sigma_{\text{sca}}^{\text{QST}} = \frac{\pi^2}{2} r x^3\left|\frac{m^2-1}{m^2+1}\right|^2, \tag{9}$$

$$\sigma_{\text{ext}}^{\text{QST}} = 2\pi r x\ \text{Im}\left(\frac{m^2-1}{m^2+1}\right) + \sigma_{\text{sca}}^{\text{QST}}. \tag{10}$$

In the limit $x \to 0$, $|m|x \to 0$, the QST cross-sections (7) – (10) are recovered by Taylor-expanding Mie expressions.

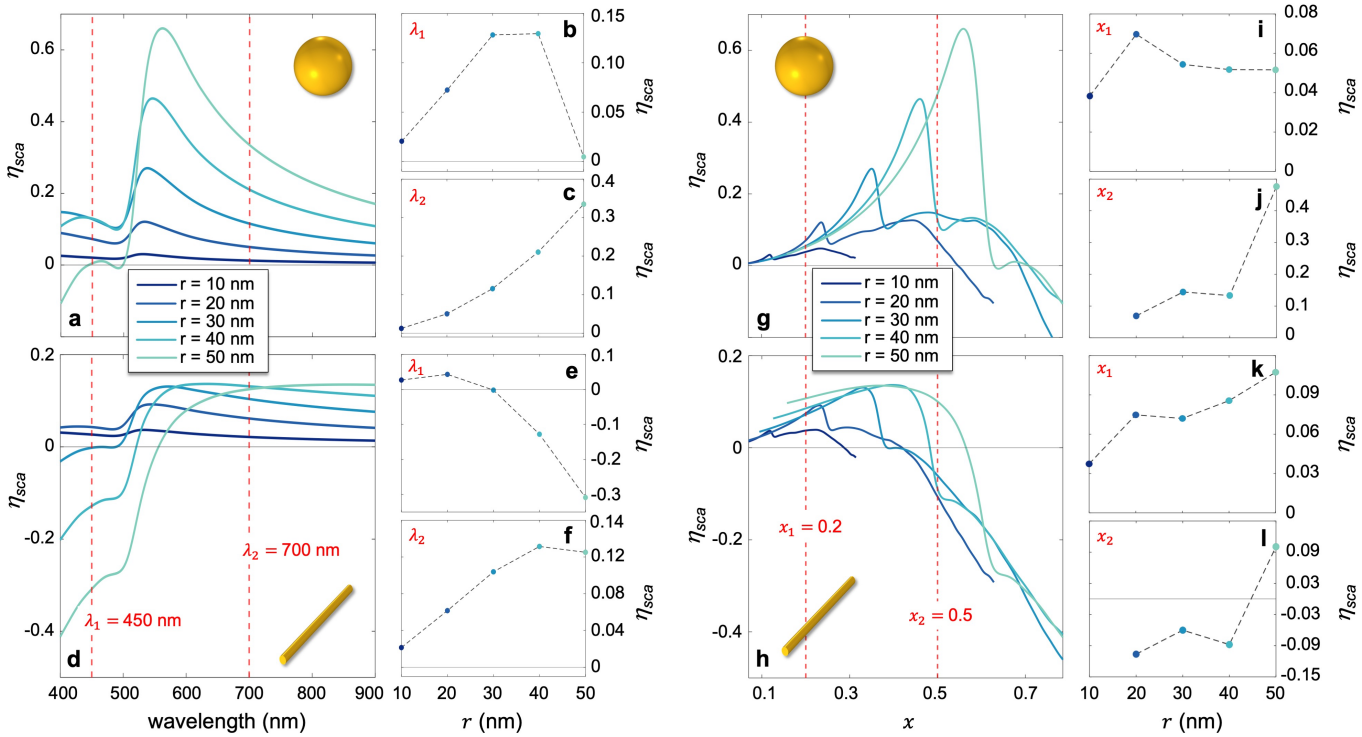


FIG. 1. **Error estimation in QST**. (a) Spectrum of the metric of the error estimation in the scattering cross-section $\eta_{\rm sca}$, quantifying the error introduced by the QST approximation when compared to exact results from Mie theory for a 3D spherical Au NP of radius $r$ (ranging from 10 to 50 nm, refer to panel legend) embedded in a homogeneous environment (air, refractive index $n_e = 1$). (b), (c) Section of panel (a) at $\lambda_1 = 450$ nm and $\lambda_2 = 700$ nm for different values of $r$. (d) Same as (a) for a cylindrical wire, modelled as a 2D structure with radius $r$. (e), (f) Section of panel (d) at $\lambda_1 = 450$ nm and $\lambda_2 = 700$ nm for different values of $r$. (g)-(l) Same as (a)-(f), as a function of the smallness parameter $x$. Note that at a given value of $x$ the evaluation of $\eta_{sca}$ for different values of radius $r$ is performed at different wavelengths.

In order to quantify the error of QST for a given configuration over a large spectral range, we defined the following metric:

$$\eta_{\rm sca} = \frac{\sigma_{\rm sca} - \sigma_{\rm sca}^{\rm QST}}{\sigma_{\rm sca}^{\rm QST}}, \tag{11}$$

determined from Eqs. (3) and (7) for a sphere, Eqs. (5) and (9) for a cylindrical wire.

We studied Au structures freestanding in air ($n_m$ taken from [29], while $n_e = 1$) with radii ranging from 10 to 50 nm. Results are shown in Fig. 1. The spectra of the metric $\eta_{\rm sca}$ reveals a non-trivial scaling with the radius $r$. Precisely, $\eta_{\rm sca}$ grows monotonically with $r$, (i.e. with the radius $r$) (that is, proportional to the smallness parameter $x$ at a fixed wavelength), in the long-wavelength range; conversely, for shorter wavelengths, $\eta_{\rm sca}$ initially grows with $r$ for small radii, but at a definite value of the radius $r$, which is specific for each structure, this trend is reversed and $\eta_{\rm sca}$ drops with increasing $r$, changing sign and eventually growing again in modulus (refer to panels (b), (c) and (e), (f) in Fig. 1). QST thus switches from underestimating to overestimating the scattering cross-section in the spectral region between 400 and 500 nm. Such a counterintuitive trend can be further highlighted when $\eta_{\rm sca}$ is evaluated as a function of the $x$ parameter, as shown in Figs. 1g and 1h. Note that for any of the radii under consideration, $\eta_{\rm sca}$ does not exhibit a monotonic increase with $x$, rather it starts increasing, reaches a peak value and then decreases and changes sign, for both spherical NPs and nanowires. Figures 1i, 1k and 1j, 1l further detail how the trend of $\eta_{\rm sca}$ with $r$ is not monotonic even when evaluated at a given value of $x$ (here 0.2 or 0.5).

To gain an insight on these features we analysed the series in (3) and (5). By Taylor expanding the Mie coefficients around $x = 0$, $|m|x = 0$, and considering their square modulus, one can find higher order corrections to the leading order term, i.e. to QST. For the sphere, corrections up to the third order can all be found by expanding the $a_1$ coefficient, which corresponds to the dipolar coefficient in the multipolar decomposition of the fields [30]. The expansion reads

$$|a_1|^2 = \frac{4}{9}\left|\frac{m^2-1}{m^2+2}\right|^2 x^6 + \tag{12a}$$

$$+ \frac{8}{15}\left|\frac{m^2-1}{m^2+2}\right|^2 \mathrm{Re}\left(\frac{m^2-2}{m^2+2}\right) x^8 + \tag{12b}$$

$$- \frac{16}{27}\left|\frac{m^2-1}{m^2+2}\right|^2 \mathrm{Im}\left(\frac{m^2-1}{m^2+2}\right) x^9 + o(x^9). \tag{12c}$$

Also for the cylindrical wire, corrections up to the second order can be found by expanding the $c_1$ term:

$$|c_1|^2 = \frac{\pi^2}{16}\left|\frac{m^2-1}{m^2+1}\right|^2 x^4 + \tag{13a}$$

$$+ \frac{\pi^2}{16}\left|\frac{m^2-1}{m^2+1}\right|^2 \mathrm{Re}\left(\frac{m^2-1}{m^2+1}\right) x^6 \ln x + \tag{13b}$$

$$+ o(x^6 \ln x). \tag{13c}$$

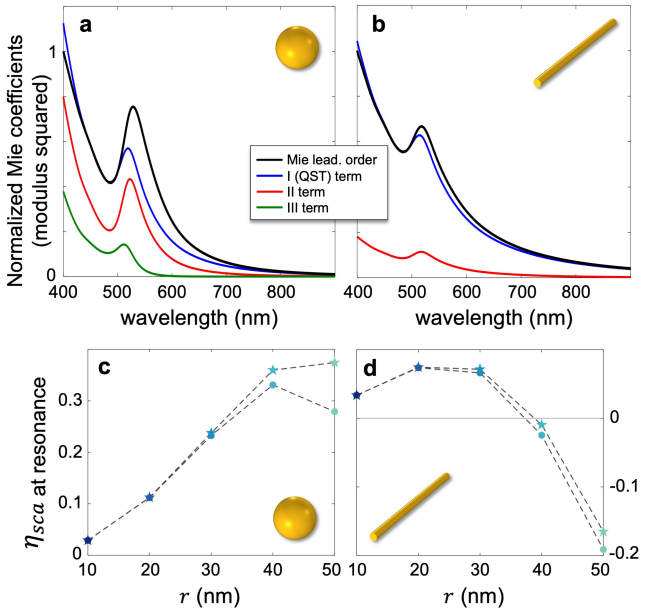


FIG. 2. **Mie coefficient expansion and QST error at resonance.** (a) The modulus squared of the leading (dipolar) order $a_1$ of the Mie coefficients for a Au spherical NP of radius r = 50 nm (black curve, left hand side of Eq. 12a) is compared to the its Taylor expansion. Spectra of the first, i.e. QST, term (blue curve, right hand side of Eq. 12a), second (red, Eq. 12b) and third (green, Eq. 12c) term are displayed. Note the short-wavelength regime (highest smallness parameter), where the QST term is greater than, i.e. overestimates, the full Mie dipolar contribution. (b) Modulus squared of the $c_1$ coefficient (black curve, left hand side of Eq. 13a) for a cylindrical wire, modeled as a 2D structure with radius r = 30 nm. First (QST, blue curve, right hand side of Eq. 13a) and second (red curve, Eq. 13b) terms of the expansion are shown. (c-d) Error of QST evalutated at the plasmonic resonance for (c) spherical NPs and for (d) cylindrical wires. The metric provided by Eq. (11) was employed with $\sigma_{sca}$ and $\sigma_{sca}^{QST}$ evaluated either at their respective peak wavelengths (stars) or at the same wavelength, corresponding to the QST scattering peak (dots).

Note that the reliability of the expansion in estimating the exact Mie coefficient (and therefore the exact cross-sections) is limited to the parameter space regions where $x$ and $|m|x$ are smaller than 1 (for the sphere) or than $1/e$ (for the cylindrical wire). Such difference stems from the specific form of the dipolar coefficient (either $a_1$ or $c_1$, respectively), which depends on the particular geometry of the scatterer. As a result, different structures entail different levels of strictness on the conditions on $x$ and $|m|x$. If $x$, $|m|x$ are not within the prescribed limits, it is not granted that the sum of the first terms on the right hand side of Eq. (12) and (13) is a good approximation of the respective quantities on the left hand side.

Moreover, for the parameters here analysed, the only relevant contribution to the cross-sections comes from the dipolar coefficient. Therefore, QST error must arise from a quantitative failure in predicting the dipole moment of structures which essentially behave as dipoles. Consequently, features of the discrepancy between QST and Mie theory illustrated in Fig. 1 should be retrieved by examining the full dipolar contribution (either $|a_1|^2$ or $|c_1|^2$) against the first term in its Taylor expansion, i.e. the QST term.

In Fig. 2 this comparison is displayed for a sphere with radius $r = 50$ nm and a cylindrical wire of radius $r = 30$ nm. For these radii, $|m|x \sim 1$ over the entire spectrum, making the expansion unreliable. Indeed, in the short-wavelength region of the spectrum, the QST term overestimates the exact dipolar contribution. This is consistent with and explains the change of sign in $\eta_{\mathrm{sca}}$ in Fig. 1. Moreover, note that the mismatch between the spectral peak of the Mie dipolar term (black trace in Figs. 2a-b) and that of the QST prediction (blue trace in Figs. 2a-b) already well captures the characteristic redshift of the plasmonic resonance with increasing size.

We also evaluated the QST error at the plasmonic resonance wavelength. The results are reported in Fig. 2c and 2d, respectively for spherical NPs and cylindrical nanowires, as a function of their radius $r$. Note that $\eta_{\mathrm{sca}}$ exhibits very different behaviors for the two geometries: for spheres, $\eta_{\mathrm{sca}}$ essentially increases with $r$, even though not always monotonically (depending on the way the $\eta_{\mathrm{sca}}$ is evaluated, see caption of Fig. 2), whereas for wires the error starts increasing, then reaches a peak value and decreases with a change in sign for larger radii.

Importantly, the accuracy of QST does not only depend on the geometry of the scatterer, but also on the conditions of interaction with electromagnetic radiation. Anisotropic structures such as wires with elliptical section are among the simplest geometries suitable to investigate QST limits in relation to excitation conditions. We thus analysed the optical response of Au elliptical wires with semi-axis $a$ and $b$, aligned (with major axis) along $x$ or $y$ directions, freestanding in air ($n_m$ from [29], $n_e = 1$). Plane wave illumination with in-plane polarisation has been considered, with the electric field either parallel or perpendicular to the NP major axis, in order to excite the Longitudinal or the Transverse Plasmon Resonance (LPR/TPR), respectively. Numerical results (obtained via FEM analysis, implemented using the commercial software COMSOL Multiphysics 5.6) are compared with the QST predictions.

For the considered geometry, the corresponding QST cross-sections read as follow (details on formulae here

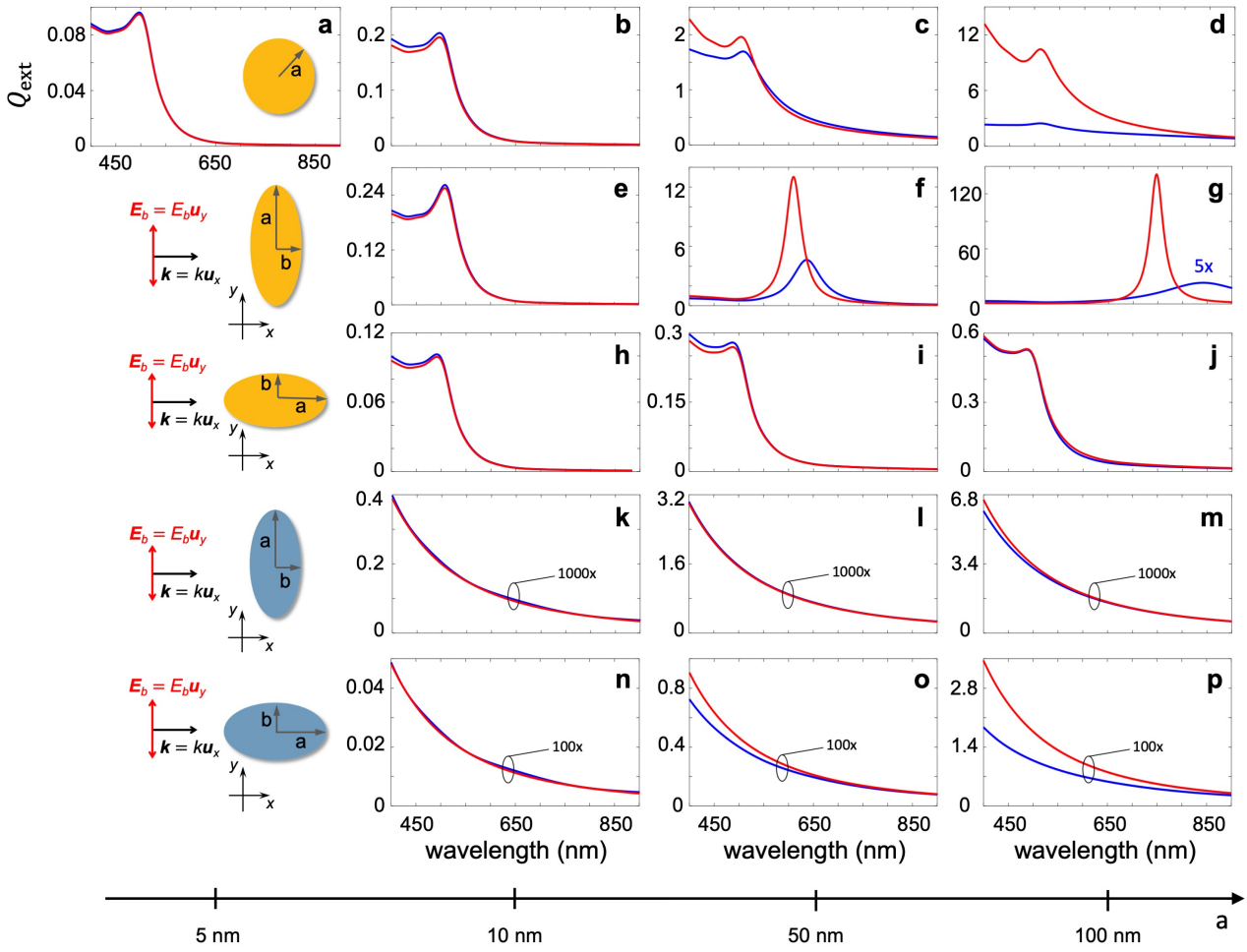


FIG. 3. **Numerical and QST extinction efficiencies for anisotropic wires.** (a-d) Comparison between extinction efficiency spectra obtained either from numerical FEM simulations (blue curves) or QST analytical formulae (red curves) for a Au cylindrical wire embedded in a homogeneous dielectric medium (refractive index $n_m = 1$) with radius equal to 5 nm (a), 10 nm (b), 50 nm (c), 100 nm (d) upon excitation of a linearly polarised plane wave with electric field along the $y$-direction. (e-g) Same as (b-c) for an elliptical wire with semi-axis along the $x$-direction fixed and equal to 5 nm, semi-axis along the $y$-direction equal to 10 nm (e), 50 nm (f), 100 nm (g). (h-j) Same as (a-c) for an elliptical wire with semi-axis along the $y$-direction fixed and equal to 5 nm, semi-axis along the $x$-direction equal to 10 nm (h), 50 nm (i), 100 nm (j). Note that (a) shows the case for a degenerate elliptical wire of equal semi-axes. (k-p) Same as (e-j) for a dielectric wire consisting of fused-silica (permittivity 2.10).

below are provided in the Methods):

$$\sigma_{\mathrm{sca}}^{\mathrm{QST}} = \frac{k^3}{8}\pi^2 a^2 b^2 (a+b)^2 \left| \frac{m^2-1}{am^2+b} \right|^2, \qquad (14)$$

$$\sigma_{\mathrm{ext}}^{\mathrm{QST}} = k\pi ab(a+b)\ \mathrm{Im}\left( \frac{m^2-1}{am^2+b} \right) + \sigma_{\mathrm{sca}}^{\mathrm{QST}}. \qquad (15)$$

Efficiencies are then defined as the ratio between cross-sections and the cross-sectional area of the structure. The smallness parameter $x$ is commonly defined as for the cylindrical wire, substituting $r$ with the major semi-axis of the elliptical section. The results for wires with varying aspect ratios are shown in Fig. 3. For comparison, spectra obtained for cylindrical wires in the same range of the smallness parameter (i.e. with radius equal to the ellipse major semi-axis) are displayed, starting from the degenerate case $a = b$ (Fig. 3a).

A first comparison between cylindrical and elliptical wires in the LPR configuration (panels a – g in Fig. 3) shows that structures with the same smallness parameter have remarkably different features with respect to the QST accuracy: QST fails much sooner (that is, at lower values of $x$) for the elliptical LPR configuration than for the corresponding cylindrical case. Specifically, QST is not able to quantitatively capture the scaling of the resonance spectral position with the aspect ratio of the structure, which is known to be caused by depolarization effects [31], and consistently overestimates the ex-

tinction efficiency. Moreover, as illustrated by panels e – j in Fig. 3, elliptical wires with the same smallness parameter, but orthogonal orientations with respect to the polarisation of the incident field, exhibit very different behaviour. Contrary to the LPR (panels e – g in Fig. 3), under TPR excitation (panels h – j in Fig. 3), the efficiency predicted by QST remains remarkably accurate as the major semi-axis is increased from 10 to 100 nm. It

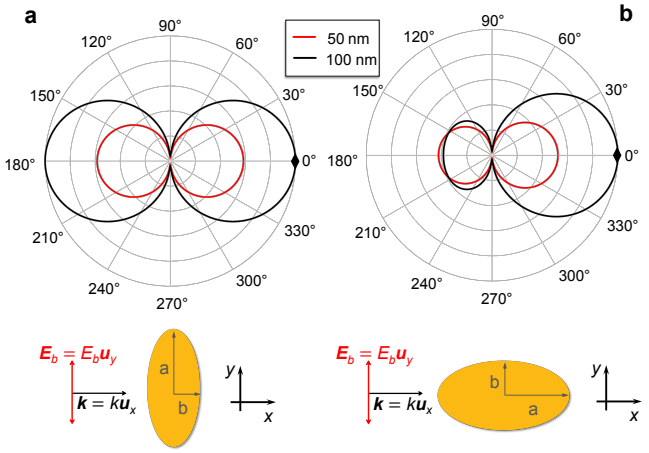


FIG. 4. **Diffraction pattern from anisotropic wires.** Far-field scattering intensity pattern evaluated via full-wave simulations at the scattering resonance $\lambda_{sca}$ of a Au elliptical wire in air with semi-axis along $x$ equal to 5 nm, semi-axis along $y$ equal either to 50 nm (red curve, $\lambda_{sca} = 640$ nm) or to 100 nm (black curve, $\lambda_{sca} = 840$ nm). Quantities are normalised to the intensity scattered at 0° for the geometry with the highest aspect ratio marked by black diamond on the horizontal axis. (b) Same as (a) for an elliptical wire with semi-axis along $y$ fixed and equal to 5 nm, semi-axis along $x$ equal either to 50 nm (red curve) or to 100 nm (black). The scattering resonance spectral position is the same for the two structures ($\lambda_{sca} = 510$ nm).

is interesting to compare the results of Figs. 3e-3g and Figs. 3h-3j with those retrieved for dielectric nanowires (fused silica), under same excitation conditions and size of structures. The results are reported in Figs. 3k-3m and 3n-3p. Note that in this case, where the structure cannot exhibit any resonant feature due to a relatively low optical density (preventing the onset of Mie resonances), the accuracy of QST prediction again depends on the orientation of cylindrical cross-section with respect to incoming wave. However, the situation is now reversed compared to the case of plasmonic nanostructures: the QST starts departing from full-wave calculations when the major axis is parallel to the wave-vector and not to the electric field of the background wave. The peculiar trend observed for the plasmonic configuration was further investigated by examining the angular patterns of scattered intensity at resonance in the LPR vs TPR cases for the two wires of highest aspect ratio, with minor semi-axis equal to 5 nm and major semi-axis equal to 50 and 100 nm, respectively. Results are shown in Fig. 4.

Analysis of the far-field intensity patterns confirms the physical intuition that radiation in the LPR case is mostly of dipolar nature (Fig. 4a). Viceversa, in the TPR configuration, forward-scattering is enhanced with respect to back-scattering (Fig. 4b), and the resulting angular spectrum proves the relevance of other multipolar contributions to the scattered intensity, which indicates the onset of retardation effects. Despite this fact, QST remains accurate for the TPR configuration up to larger values of the smallness parameter, meaning that, incidentally, retardation effects have very limited impact on the estimation of the total scattered power.

Thus, it is confirmed that the error of the QST approximation resides in its failure to accurately predict the induced dipolar moment. The commonly accepted definition of the smallness parameter does not capture this feature, which depends on the polarisation of the incident light. This concept should be reframed: the smallness parameter can't be viewed as an *a priori* property of the scatterer, instead it should be defined according to the excitation conditions. For plasmonic nanoparticles, this can be done by replacing the characteristic size (i.e. the maximum distance between two points inside the nanostructure) with the size of the projection of the nanoobject along the direction of the background field.

Another misconception about QST is related to the homogeneity of the phase and modulus of the electric field across the structure, which is commonly considered to be a key aspect in QST applicability limits, as summarised in the condition of Eq. (2). To investigate this issue, we examined the pattern of the norm and direction of the electric field inside two-dimensional nanostructures for the following pivotal configurations: a cylindrical wire with $r = 5$ nm; an elliptical wire with minor semi-axis equal to 5 nm and major semi-axis equal to 100 nm, both in the LPR and the TPR excitation conditions. The results are displayed in Fig. 5. The field inside the small cylindrical wire has an almost constant phase throughout the structure, and can be considered homogeneous in modulus up to a 10% variation between the left and right hand of the scatterer (Fig. 5a). Here QST predictions are in excellent agreement with full-wave numerical calculations. However, the field is comparably uniform also in elliptic wire for the LPR case (Fig. 5b), where viceversa QST is no longer reliable, as discussed above. Most interestingly, the elliptic wire in the TPR configuration, that have been demonstrated to be well described by QST calculations, exhibits significant spatial inhomogeneity of the resonant field, undergoing 180° phase shift from the left to the right side of the structure (Fig. 5c). On the basis of these results, it can be stated that the condition on the uniformity of the fields inside plasmonic nanoscatterers is not necessary to guarantee that QST approximation holds its reliability.

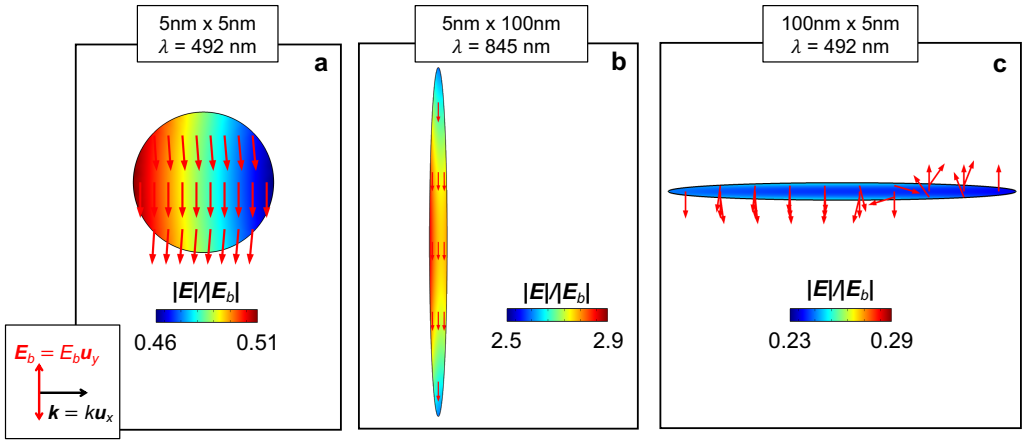


FIG. 5. **Electric field spatial distribution.** (a) 2D map of the spatial distribution of the electric field (time average) norm across a Au cylindrical wire in air of radius $r = 5$ nm evaluated at resonance ($\lambda = 492$ nm). Red arrows show the instantaneous polarisation direction of the electric field. (b) Same as (a) for an elliptical wire with semi-axis along the $x$-direction fixed and equal to 5 nm, semi-axis along the $y$-direction equal to 100 nm, evaluated at the LPR ($\lambda = 845$ nm). (c) Same as (b) for an elliptical wire with semi-axis along the $y$-direction fixed and equal to 5 nm, semi-axis along the $x$-direction equal to 100 nm, evaluated at the TPR ($\lambda = 492$ nm). Note the change in the phase of the electric field across the nano-ellipse.

## II. METHODS

### A. Mie theory implementation

To derive Mie expressions for the scattering cross-sections in Eqs.(3),(5), we developed MATLAB code implementing the following formulas for the Mie coefficients [22]:

$$a_n = \frac{m\psi_n(mx)\psi_n'(x) - \psi_n(x)\psi_n'(mx)}{m\psi_n(mx)\xi_n'(x) - \xi_n(x)\psi_n'(mx)}, \tag{16}$$

$$b_n = \frac{\psi_n(mx)\psi_n'(x) - m\psi_n(x)\psi_n'(mx)}{\psi_n(mx)\xi_n'(x) - m\xi_n(x)\psi_n'(mx)}, \tag{17}$$

$$c_n = \frac{mJ_n(mx)J_n'(x) - J_n(x)J_n'(mx)}{mJ_n(mx)H_n'^{(1)}(x) - H_n^{(1)}(x)J_n'(mx)}. \tag{18}$$

Here $m$ is the ratio of the metal and environment refractive indexes, $\psi_n(x) = xj_n(x)$ and $\xi_n(x) = xh_n^{(1)}(x)$ are the Riccati-Bessel functions, and $J_n$ and $H_n^{(1)}$ are the Bessel and Hankel functions of the first kind, respectively.

### B. QST for plasmonic nanowires with elliptical cross-section

We derived the polarizability of an infinite wire with elliptical cross-section by considering a standard 2D cartesian frame of reference, centered on the elliptical section of the nanowire, with major semi-axis $a$ along the horizontal ($x$) axis and minor semi-axis $b$, excited by a plane wave propagating along $x$ and linearly polarised along the $y$-axis.

The electromagnetic problem can be formulated in elliptic coordinates $(\mu, \nu)$, which are linked to the cartesian -ones $(x, y)$ via the following relations:

$$x = f\cosh\mu\cos\nu, \tag{19}$$

$$y = f\sinh\mu\sin\nu. \tag{20}$$

Here $f$ is the $x$-coordinate of one of the foci, and is defined such that $f^2 = a^2 - b^2$; $\mu$ ranges from 0 to $\infty$ and $\nu$ from 0 to $2\pi$. Lines of constant $\mu$ are concentric ellipses, lines of constant $\nu$ are branches of hyperbola with foci on the horizontal axis. The edge of the elliptical section is described by the equation $\mu = \tanh^{-1}(b/a) =: \bar{\mu}$.

QST approach consists in solving the problem described by the Laplace equation for the electrostatic potential $\Phi$, i.e. $\nabla^2\Phi = 0$. Any solution of this equation can be written as a linear combination of elliptical harmonics $\{\Phi_n\}_{n=0,1,\ldots}$ defined as follows:

$$\Phi_n = \begin{cases} A + B\mu & \text{if } n = 0, \\ (A_n\sinh n\mu + B_n\cosh n\mu)\sin n\nu + & \\ + (A_n'\sinh n\mu + B_n'\cosh n\mu)\cos n\nu & \text{otherwise.} \end{cases} \tag{21}$$

The background potential due to the incident field $\mathbf{E_b} = E_0\hat{\mathbf{u}}_\mathbf{y}$ can be written as $\Phi_b = -E_b f\sinh\mu\sin\nu$. Then the total potential is $\Phi = \Phi_b + \Phi_s$, with $\Phi_s$ the scattered potential. For simplicity we seek for the fundamental solution with $n = 1$, so that the total potential outside and inside the scatterer can be written, respectively, as:

$$\Phi_{\text{ext}} = \Phi_b + Ce^{-\mu}\sin\nu, \tag{22a}$$

$$\Phi_{\text{int}} = D\sinh\mu\sin\nu. \tag{22b}$$

Note that according to Eq. (22a), $\Phi_{\text{int}}$ corresponds to a uniform electric field inside the scatterer. In above equations, $C$ and $D$ are constants to be determined through

the boundary conditions at the surface of the scatterer, i.e. continuity of $\partial\Phi/\partial\nu$ and of $\varepsilon\partial\Phi/\partial\mu$ in $\mu=\bar{\mu}$. Therefore, the scattered potential is:

$$\Phi_s = Ce^{-\mu}\sin\nu = \frac{\varepsilon_m-\varepsilon_e}{\varepsilon_m a+\varepsilon_e b}\frac{ab}{a-b}fE_b e^{-\mu}\sin\nu. \quad (23)$$

At large distance from the origin, $\nu$ corresponds to the angular $\theta$ coordinate, and $r\sim\frac{f}{2}e^{\mu}$. As a result, in this regime $\Phi_s$ can be written as

$$\Phi_s \underset{r\to\infty}{=} \frac{p\sin\theta}{2\pi\varepsilon_e\varepsilon_0 r}, \quad (24)$$

where $p$ is the modulus of the induced dipole moment, expressed as

$$\mathbf{p} = \pi\varepsilon_0 ab\frac{\varepsilon_m-\varepsilon_e}{\varepsilon_m a+\varepsilon_e b}(a+b)\varepsilon_e\mathbf{E_b}. \quad (25)$$

Thus, the elliptic $y$-polarizability $\alpha_y$ can be defined by setting $\mathbf{p}=\alpha_y\varepsilon_e\mathbf{E_b}$.

Having defined the absorption cross-section $\sigma_{\text{abs}}$ as the ratio between the absorbed power and the intensity of the incident wave, it is easy to show, from Poynting theorem [30], that

$$\sigma_{\text{abs}}^{\text{QST}} = \frac{k}{\varepsilon_0}\text{Im}\left(\alpha_y\right). \quad (26)$$

For the elliptical case, this expression corresponds to the first term on the right hand side of Eq. (15). On the other hand, the cylindrical wire expression can be evaluated as the degenerate case, setting $a=b=r$. In this way, the first term on the right hand side of Eq. (10) is recovered.

Since QST is at leading order an electrostatic theory, it is necessary to account for higher order corrections in order to compute the scattering cross-section. To perform this task, it is possible to start from the description of a generic system of localized charges and currents varying sinusoidally in time with the same frequency of the incident plane wave, $\rho(\mathbf{r},t)=\rho(\mathbf{r})e^{-\text{i}\omega t}$ and $\mathbf{j}(\mathbf{r},t)=\mathbf{j}(\mathbf{r})e^{-\text{i}\omega t}$. The 2D vector potential in the Lorentz gauge [30] can be recast as

$$\mathbf{A}(\mathbf{r},t) = \text{i}\frac{\mu_0}{4}e^{-\text{i}\omega t}\int \text{d}^2\mathbf{r}'\mathbf{j}(\mathbf{r}')H_0^{(1)}(k|\mathbf{r}-\mathbf{r}'|), \quad (27)$$

where $H_0^{(1)}$ is the 0-th order Hankel function of the first kind and $k=\omega n_e/c=2\pi n_e/\lambda$. In the radiation zone, where $\mathbf{r}$ is such that $d\ll\lambda\ll r$ (with $d$ the characteristic dimension of the oscillating source), the Hankel function can be expanded, and, noting that continuity equation implies $-\text{i}\omega\int\text{d}^2\mathbf{r}'\rho(\mathbf{r}')\mathbf{r}'=-\text{i}\omega\mathbf{p}$, we get:

$$\mathbf{A}(\mathbf{r},t) \simeq \frac{\mu_0 e^{-\text{i}\frac{\pi}{4}}}{4}\sqrt{\frac{2}{\pi}}e^{-\text{i}\omega t}\frac{e^{\text{i}kr}}{\sqrt{kr}}\omega\mathbf{p}. \quad (28)$$

The far field expression of the magnetic and electric scattered fields are then retrieved as:

$$\mathbf{H}_s = H\hat{\mathbf{u}}_\mathbf{z} = \frac{1}{\mu_0}\partial_x A\hat{\mathbf{u}}_\mathbf{z}, \quad (29a)$$

$$\mathbf{E}_s = \frac{\text{i}}{k}\sqrt{\frac{\mu_0}{\varepsilon_0\varepsilon_e}}\left(\partial_y H\hat{\mathbf{u}}_\mathbf{x}-\partial_x H\hat{\mathbf{u}}_\mathbf{y}\right). \quad (29b)$$

Then, the total scattered power is computed as:

$$P_{\text{sca}} = \int_0^{2\pi}\mathbf{S}\cdot\hat{\mathbf{u}}_\mathbf{r}\,r\text{d}\theta = \frac{\mu_0}{16}\omega^3|\mathbf{p}|^2, \quad (30)$$

with $\mathbf{S}=(1/2)\text{Re}\left(\mathbf{E}_s\times\mathbf{H}_s^*\right)$ the Poynting vector of the scattered field. The scattering cross-section is obtained by dividing $P_{\text{sca}}$ by the incident intensity $I_0=\frac{1}{2}\varepsilon_0 n_e c|\mathbf{E_b}|^2$ and using Eq. (25) to make $|\mathbf{p}|^2$ explicit:

$$\sigma_{\text{sca}}^{\text{QST}} = \frac{k^3}{8\varepsilon_0^2}|\alpha_y|^2. \quad (31)$$

This equation corresponds to Eq. (14), and its sum with Eq. (26) gives Eq. (15). Again, the cylindrical wire case can be recovered as the degenerate case.

### C. Full-wave numerical analysis

The full-vectorial 2D scattering problem upon excitation with a monochromatic plane wave having in-plane polarisation was implemented for the elliptical and cylindrical nanowires shown in Fig. 3.

The considered domain was a circle of radius $r_{\text{ext}}=900$ nm with perfectly matched layers of 500 nm thickness. We performed finite element methods analysis to solve for the scattered electric and magnetic fields, employing a commercial software, Comsol Multiphysics 5.6. The absorption cross-section is computed, according to Poynting theorem, as follows [30]:

$$\sigma_{\text{abs}} = \frac{1}{2I_0}\int_{Au}\text{Re}\left(\mathbf{j}\cdot\mathbf{E}^*\right)\text{d}A, \quad (32)$$

where $I_0$ is the incident intensity, $\mathbf{j}$ is the current density, $\mathbf{E}$ is the total electric field (i.e. sum of the background and scattered fields) and the integration $\int_{Au}\text{d}A$ is performed on the Au nanowire surface. Notice that, due to the fact that our model is 2D, the cross-section is a length, not an area.

The formula for the scattering cross-section is instead

$$\sigma_{\text{sca}} = \frac{1}{2I_0}\int_\Gamma\text{Re}\left(\mathbf{E}_s\times\mathbf{H}_s^*\right)\cdot\hat{\mathbf{u}}_\mathbf{r}\text{d}l \quad (33)$$

where $\mathbf{E}_s$ and $\mathbf{H}_s$ are the scattered fields, $\Gamma$ is a circle surrounding the nanowire, and $\hat{\mathbf{u}}_\mathbf{r}$ is the outward-pointing vector in the radial direction, which is normal to the circle itself.

The extinction cross-section is then derived as the sum $\sigma_{\text{ext}}=\sigma_{\text{abs}}+\sigma_{\text{sca}}$.

Far-field computations from near-fields have also been performed in Comsol (implementing to the Stratton-Chu formula [22]) to extract the radiation patterns shown in Fig. 4.

## CONCLUSIONS

We investigated the limits of QST by studying gold nanostructures freestanding in air.

In the first part of this work, we computed scattering spectra of spherical nanoparticles and cylindrical nanowires of various radii using Mie scattering theory and compared the results with the QST predictions. We observed a non-trivial, non-monotonic behaviour of $\eta_{\mathrm{sca}}$ as a function of the smallness parameter at short wavelengths. In order to investigate this trend, we compared the dipolar contribution to the scattering cross-section from Mie expansion with its leading order, corresponding to the QST term. We find that the non-monotonic trend of $\eta_{\mathrm{sca}}$ can be ascribed to the specific form of the Mie dipolar coefficient.

From a physical point of view, these facts can be interpreted as follows: QST fails quantitatively in estimating the dipole moment of the nanostructures as they grow in size, even when the scatterers are still behaving as dipoles. Furthermore, the conditions $x \ll 1$ and $|mx| \ll 1$ are only sufficient conditions for the accuracy of QST in predicting the optical response of a system; even more, 3D geometries and 2D geometries with circular cross-sections having the same radius entail different levels of strictness in these conditions.

In the second part of this work, we concentrated on nanowires with elliptical cross-section. We performed numerical simulations using finite elements methods and compared the extracted extinction spectra with the QST prediction, again for a broad range of sizes and two different polarisation conditions, exciting in turn TPR and LPR in the same structures. Nanowires revealed opposite behaviour with respect to QST accuracy upon excitation of TPR versus LPR. In TPR configuration, indeed, QST holds its validity for much larger values of the smallness parameter $x$ compared to the LPR case.

Angular patterns of the scattered intensity confirm that nanowires with relatively high values of $x$ still radiate as electric dipoles in the LPR configuration, whereas in the TPR case other multipolar contributions become relevant, enhancing forward-scattering with respect to back-scattering at resonance. Therefore, the goodness of QST predictions in the TPR vs LPR case confirms that the error of this approximation resides in the discrepancy between the *predicted* (static) and the true induced dipolar moment, which is due to retardation effects, completely disregarded in the quasi-static regime. Moreover, in the TPR configuration, the reliability of QST is not affected by the non-uniformity of the field inside the nanowire. For example, QST predictions are still fairly accurate in the extreme case, corresponding to a major semi-axis of 100 nm, where the field undergoes a 180° phase shift from one side of the structure to the other. Indeed, uniformity of phase and modulus of the electric field is required to exactly reproduce the configuration of the quasi-static field; it is not needed, on the other hand, to grant accuracy in the computation of integral properties such as the extinction efficiency of the scatterer. This dispels the misconception that a necessary condition for the validity of QST approximation is the uniformity of the field inside the structure, when dealing with calculations of cross sections.

Interestingly, a detailed comparison with dielectric nanocylinders indicate that the complex scenario above detailed is peculiar to plasmonic configurations. In this case, the characteristic length to be taken into account when considering QST reliability is the one which is parallel to the polarization of incident radiation, and the smallness parameter should be defined accordingly. This provides a clear-cut support to the general idea that interaction of light with plasmonic nanoparticles is largely defined by the polarisation of light.

Finally, the generality of the assumptions under which these results have been obtained, entails that these conclusions can be easily extended to other plasmonic systems such as Ag or Al nanospheres and nanowires.

## DATA AVAILABILITY

The data that support the plots within this paper and other findings of this study are available from the corresponding authors upon reasonable request.

## COMPETING FINANCIAL INTERESTS

The authors declare no competing financial interests.


[1] P. K. Jain, X. Huang, I. H. El-Sayed, and M. A. El-Sayed, Accounts of Chemical Research **41**, 1578 (2008).
[2] H. Jans and Q. Huo, Chem. Soc. Rev. **41**, 2849 (2012).
[3] Y. Hong, Y.-M. Huh, D. S. Yoon, and J. Yang, Journal of Nanomaterials **2012**, 1 (2012).
[4] J. R. Mejía-Salazar and O. N. Oliveira, Chemical Reviews **118**, 10617 (2018).
[5] C. Clavero, Nature Photonics **8**, 95 (2014).
[6] X. Zhang, Y. L. Chen, R.-S. Liu, and D. P. Tsai, Reports on Progress in Physics **76**, 046401 (2013).
[7] C. Wang and D. Astruc, Chem. Soc. Rev. **43**, 7188 (2014).
[8] T. Labouret, J.-F. Audibert, R. B. Pansu, and B. Palpant, Small **11**, 4475 (2015).
[9] E. Cortés, L. V. Besteiro, A. Alabastri, A. Baldi, G. Tagliabue, A. Demetriadou, and P. Narang, ACS Nano **14**, 16202 (2020).
[10] M. Moskovits, Journal of Raman Spectroscopy **36**, 485 (2005).
[11] P. Mosier-Boss, Nanomaterials **7**, 142 (2017).

[12] M. I. Stockman, Journal of Optics **12**, 024004 (2010).
[13] A. Pors, O. Albrektsen, I. P. Radko, and S. I. Bozhevolnyi, Scientific Reports **3**, 2155 (2013).
[14] L. H. Nicholls, F. J. Rodríguez-Fortuño, M. E. Nasir, R. M. Córdova-Castro, N. Olivier, G. A. Wurtz, and A. V. Zayats, Nature Photonics **11**, 628 (2017).
[15] A. Schirato, M. Maiuri, A. Toma, S. Fugattini, R. Proietti Zaccaria, P. Laporta, P. Nordlander, G. Cerullo, A. Alabastri, and G. Della Valle, Nature Photonics **14**, 723 (2020).
[16] A. V. Zayats, I. I. Smolyaninov, and A. A. Maradudin, Physics Reports **408**, 131 (2005).
[17] S. Lal, S. Link, and N. J. Halas, Nature Photonics **1**, 641 (2007).
[18] M. Pelton, J. Aizpurua, and G. Bryant, Laser & Photonics Reviews **2**, 136 (2008).
[19] M. I. Stockman, et al., Journal of Optics **20**, 043001 (2018).
[20] S. V. Boriskina, et al., Journal of Optics **18**, 073004 (2016).
[21] G. Mie, Annalen der Physik **330**, 377 (1908).
[22] C. F. Bohren and D. R. Huffman, *Absorption and Scattering of Light by Small Particles* (Wiley, 1998).
[23] E. Stefan Kooij and B. Poelsema, Phys. Chem. Chem. Phys. **8**, 3349 (2006).
[24] F. Wang and Y. R. Shen, Phys. Rev. Lett. **97**, 206806 (2006).
[25] G. Della Valle, T. Søndergaard, and S. I. Bozhevolnyi, Phys. Rev. B **79**, 113410 (2009).
[26] J. M. Nápoles-Duarte, M. A. Chavez-Rojo, M. E. Fuentes-Montero, L. M. Rodríguez-Valdez, R. García-Llamas, and J. A. Gaspar-Armenta, Journal of Optics **17**, 065003 (2015).
[27] J. Yang, C. Sauvan, A. Jouanin, S. Collin, J.-L. Pelouard, and P. Lalanne, Opt. Express **20**, 16880 (2012).
[28] A. Dutta, V. Tiainen, and J. J. Toppari, in *3RD INTERNATIONAL CONFERENCE ON CONDENSED MATTER AND APPLIED PHYSICS (ICC-2019)* (AIP Publishing, 2020).
[29] P. B. Johnson and R. W. Christy, Physical Review B **6**, 4370 (1972).
[30] J. Jackson, *Classical electrodynamics* (Wiley, New York, 1999).
[31] R. Yu, L. M. Liz-Marzán, and F. J. G. de Abajo, Chemical Society Reviews **46**, 6710 (2017).